*sustainability*

MDPI

*Article*

# A Multi-Field Coupled PEMFC Model with Force-Temperature-Humidity and Experimental Validation for High Electrochemical Performance Design

**Zhiming Zhang [1,*], Zhihao Chen [1], Kunpeng Li [1], Xinfeng Zhang [2], Caizhi Zhang [3] and Tong Zhang [1]**

[1] School of Automotive Studies, Tongji University, Shanghai 201804, China; 2133563@tongji.edu.cn (Z.C.); 1632815@tongji.edu.cn (K.L.); tzhang@tongji.edu.cn (T.Z.)
[2] School of Information and Electrical Engineering, Zhejiang University City College, Hangzhou 310015, China; zxf@zucc.edu.cn
[3] College of Mechanical and Vehicle Engineering, Chongqing University, Chongqing 400044, China; czzhang@cqu.edu.cn
* Correspondence: zhangzm@tongji.edu.cn

**Abstract:** PEMFCs (Proton Exchange Membrane Fuel Cells) are commonly used in fuel cell vehicles, which facilitates energy conversation and environmental protection. The fuel cell electrochemical performance is significantly affected by the contact resistance and the GDL (Gas Diffusion Layer) porosity due to ohmic and concentration losses. However, it is difficult to obtain the exact performance prediction of the electrochemical reaction for a fuel cell design, resulting from the complex operating conditions of fuel cells coupled with the assembly force, operating temperature, relative humidity, etc. Considering the compression behavior of porosity and the contact pressure in GDLs, a force-temperature-humidity multi-field coupled model is established based on FEA (Finite Element Analysis) and CFD (Computational Fluid Dynamics) for the fuel cell electrochemical performance. Aside from that, the characteristics between the contact resistance and the contact pressure are measured and fitted through the experiments in this study. Finally, the numerical model is validated by the experiment of the fuel cell stack, and the error rate between the presented model and the experimentation of the full-dimensional stack being a maximum of 3.37%. This work provides important insight into the force-temperature-humidity coupled action as less empirical testing is required to identify the high fuel cell performance and optimize the fuel cell parameters in a full-dimensional fuel cell stack.

**Keywords:** PEMFC; assembly force; temperature; humidity; GDL compression; multi-field coupled model



**Citation:** Zhang, Z.; Chen, Z.; Li, K.; Zhang, X.; Zhang, C.; Zhang, T. A Multi-Field Coupled PEMFC Model with Force-Temperature-Humidity and Experimental Validation for High Electrochemical Performance Design. *Sustainability* **2023**, *15*, 12436. https://doi.org/10.3390/su151612436

Academic Editors: Andrea G. Capodaglio, Laisuo Su, Jun Huang, Shikhar Jha, Yubai Li and Biyu Jin

Received: 9 July 2023
Revised: 30 July 2023
Accepted: 14 August 2023
Published: 16 August 2023



## 1. Introduction

### 1.1. The Need for PEMFC Model

According to the IEA (International Energy Agency), the transport sector emitted 7980 million tons of $CO_2$ globally in 2022, accounting for 21.7% of total $CO_2$ emissions from fuel combustion in the world [1]. The transportation field has become an important focus in reducing oil consumption and carbon emissions [2]. To develop new energy vehicles as a breakthrough to comprehensively promote low-carbon transportation is one of the most important ways to get rid of oil dependence and reduce $CO_2$ emissions [3]. Hydrogen fuel cell electric vehicles have the advantages of zero emission, high efficiency, and long range, which is an important direction for future transport development. At present, PEMFCs are the most commonly used in fuel cell vehicles with the main advantages being low operating temperature, fast start-up, high efficiency, etc. [4].

The fuel cell stack is a key part of the fuel cell electric vehicle. As a continuous power generation source, it is responsible for providing energy to drive the vehicle. Improving

the energy efficiency and electrochemical performance of the fuel cell stack is an important goal of fuel cell research. A fuel cell stack usually consists of hundreds of single cells. A single cell includes BPPs (Bipolar Plates) and a MEA (Membrane Electrode Assembly), which is made up of GDLs (Gas Diffusion Layers), CLs (Catalyst Layers), and a PEM (Proton Exchange Membrane). The MEA and the BPP are assembled together via a certain assembly force.

The assembly force of the fuel cell stack is generally applied using point load, line load, or surface load [5]. The assembly force acting on the GDLs will affect the porosity of GDLs and the contact resistance between the GDLs and BPPs. In addition, stress concentration will occur in the GDL under the action of assembly force [6]. Different porosities will affect the dual-function of gas supply and liquid water removal capacity in fuel cells, which directly affects the concentration losses of the fuel cell performance [7,8]. The different contact resistance will affect ohmic losses of the fuel cell [9]. However, the balance between the GDL porosity and the contact resistance on the fuel cell performance under assembly force is difficult to predict and optimize. Therefore, it requires us to study the compression mechanisms of GDL involved in an effective numerical model and experimental validation. In addition, due to the coupled complexity of the operating conditions (assembly force, working temperature, relative humidity, gas supply, etc.) in fuel cells, the electrochemical performance is difficult to predict and identify, not to mention also optimize.

Due to the limitation of experimental methods and technology, it is difficult to measure the detailed data of the fuel cell components during the fuel cell working operation, such as the porosity and permeability of GDLs and the distribution of internal water content and its current density. With the development and popularization of the numerical simulation method, which has become a practical assistant to analyze these complex problems, its high efficiency, convenience, low cost, and other characteristics attract attention as more and more research is applied to analyzing fuel cell performance. How to build a fuel cell model, combined with the complex behaviors of assembly force, working temperature, relative humidity, etc., and how to facilitate the optimization of fuel cells is the focus of the current research.

### *1.2. The Effect of Assembly Force, Temperature, and Humidity on Fuel Cell Electrochemical Performance*

During the PEMFC operation process, the internal operating conditions in fuel cells involve multiple physical fields, such as the force field, thermal field, and humidity field, which are coupled with each other. The distribution of temperature, humidity, component deformations, and contact pressure directly affects the GDL porosity and contact resistance, even the electrochemical performance output of fuel cells [10].

The effect of assembly force on fuel cell stacks is mainly reflected in the porosity of GDLs and the contact pressure which affects the contact resistance between the GDLs and BPPs. The contact resistance in fuel cells is one of the main challenges to be overcome during the commercialization of fuel cells. GDL compression behavior is the key factor to controlling the contact resistance. The contact pressure on the GDL plays an important role in the performance improvement of PEM fuel cells via reducing ohmic and concentration losses [11]. The contact resistance is affected by several mechanical parameters, such as assembly force, the porosity of GDLs, and the dimensions of the GDLs and BPPs [12].

In PEMFC, the non-uniform distribution of contact pressures on the GDL leads to an increase in contact resistances, which increases ohmic losses, reduces porosity, and leads to the reaction gas concentration [13]. Therefore, it is essential to optimize the consistency and uniformity of the contact pressure of the GDL [14]. By optimizing the geometric parameters of the fuel cell assembly deign, the uniformity of the contact pressure distribution on the GDL can be increased [15]. The uniformity of the contact pressure on the GDL can be also improved by optimizing the position and size of assembly force [16].

With the increase in assembly force, the porosity and contact resistance of GDLs are continuously reduced [17]. Atyabi et al. [9] simulated a 3D multiphase model of a PEM

fuel cell to investigate the effect of assembly force on the contact resistance between the GDL and the BPP. The results show that the increase in assembly force is related to the decrease in contact resistance between the GDL and the BPP. In addition, it was found that the distribution of the electric potential and oxygen concentration is more uniform at a higher assembly force.

Assembly force also affects the electrochemical reaction concentration inside the PEMFC, which changes the output's current density. Peng et al. [18] measured the current distribution inside the fuel cell using the BPP with current sensors. The higher current passes through the reactive region with the higher contact pressure, and the current density is lower in the area with poor contact behavior. For higher output currents, the current density has a large deviation.

Under the effect of assembly force, the non-uniform porosity distribution exists in the GDL [19]. The gas flow channel will be intruded when the GDL is under the action of assembly force, which causes the GDL porosity changes [20].

The GDL porosity will also affect the transport of gas and produced water, which affects fuel cell performance. Suitable deformation for the GDL is conducive to the flow of liquid water to the channel, which reduces the accumulation of liquid water under the ribs. At the same time, the GDL porosity will affect its permeability, which is not conducive to the mass transfer in the GDL [21].

The contact resistance between the GDL and the BPP existing in PEMFC is responsible for ohmic losses during the electrochemical reactions [22]. When the assembly force increases, the contact resistance becomes smaller, but the mass transmission of fuel cells becomes weaker, leading to the increase in concentration losses [13]. An optimum PEMFC performance can be achieved by choosing an appropriate assembly force to balance the relationship between them.

Factors affecting fuel cell performance are not only assembly force, but also temperature and humidity [23]. A high fuel cell performance requires appropriate temperature and humidity [24]. During the operation of fuel cells, the temperature and humidity distribution are non-uniform and changes under different operating conditions [25]. Under the condition of low-current densities, the distribution of temperature and humidity are relatively uniform, while for high-current densities, the non-uniform distribution temperature and humidity will increase [26]. Temperature and humidity also interact with each other, which are competitive, and humidity especially has a greater impact on the temperature distribution at high-current densities [27]. At the same time, the PEMFC performance increases with the increase in temperature and humidity [28,29].

The variance in temperature and humidity will affect the MEA (Membrane Electrode Assembly) mechanical properties and cause MEA thermal and hydrated deformation [30]. By studying the force-temperature coupled model of fuel cells, it was found that the contact pressure between the MEA and the BPP increases due to thermal variance, which affects the stress distribution inside the MEA [31].

The relationship among temperature, humidity, and assembly force is not independent. For example, high temperature with high humidity obviously leads to stress concentration on the MEA; assembly force also affects the humidity distribution [32]. Liu et al. [33] established a two-dimensional fuel cell model to study the stress distribution under assembly force and found that stress concentration exists in the joint area between the gaskets and GDLs, and the maximum stress is mainly related to temperature and humidity. Under the combined action of temperature and humidity, the stress of the MEA increases, which can affect the PEM durability [34]. Studies have also shown that stress is higher at low assembly force and high humidity and temperature, which affects the fuel cell performance [35].

Ouaidat et al. [36] used a multi-physics model to optimize the fuel cell performance. A 3D finite element analysis including a full coupling of thermal-electrical-mechanical model is proposed to predict the electrical resistance of fuel cells. Zhang et al. [23] studied the performance of fuel cells using a coupled two-dimensional PEM fuel cell deformation model and a three-dimensional CFD model. The membrane deformation and PEM fuel

cell performance under different RHs (Relative Humidities) were also investigated, and medium RH values were found to achieve good fuel cell performance if the membrane swelling effect was considered. Some studies are listed in Table 1.

**Table 1.** The comparison of models.

| Author | Dimension | Influence Factor | Research Content |
|---|---|---|---|
| Liu [33] | 2D | assembly force | stress distribution |
| Bograchev [34] | 2D | assembly force, temperature, humidity | stress distribution |
| Mehrtash [35] | 2D | assembly force, humidity, current density | stress distribution |
| Mert Taş [28] | 3D | temperature, humidity | performance optimization |
| Shen [27] | 3D | temperature, humidity, current density | performance optimization |
| Ouaidat [36] | 3D | thermal, electrical, mechanical | performance optimization |
| Zhang [23] | 3D | humidity, deformation | performance optimization |

Based on these analyses, it can be seen that temperature, humidity, and assembly force all greatly affect the fuel cell electrochemical performance, which are coupled together to act on the contact pressure and the GDL porosity. However, the current studies on these factors do not take the non-uniform distribution and the dynamic variance of temperature and humidity into account. There are certain differences between the actual situation and the numerical model results, which cannot fully reflect the complex state inside the fuel cell, not to mention also optimization.

In this study, a force-temperature-humidity coupled model of the fuel cell is established using FEA and CFD methods and is finally validated by the experiments. This model considers the change of porosity and the effect of the contact pressure on the contact resistance. The main features of the coupled model can be described as follows:

(1) The model considers the effect of stress distribution on the performance by adding the effect of stress distribution on the contact resistance and the GDL porosity to the electrochemical model.
(2) The contact resistance under different contact pressure is measured via the test, which makes the simulation results closer to the reality.
(3) The polarization curve is used to calibrate model parameters, which makes the model closer to the test results.
(4) The simulation results of the model are validated by the actual stack to ensure the accuracy of the model.

The effects of assembly force, temperature, and humidity on the fuel cell performance can be predicted using the model so as to optimize the fuel cell performance. The model also takes the influence of the non-uniform distribution of temperature on the porosity and permeability of the GDL into account and uses temperature to couple assembly force and humidity together, so that the influence of assembly force, temperature, and humidity on fuel cell performance can be well understood more clearly.

## 2. Parameters Measurement

The Simulink model is based on the fuel cell stack which is used in the test. In order to make the model closer to the actual fuel cell stack, some parameters would be measured using the test. The test is mainly divided into contact resistance measurements and single cell polarization curve measurements, where the former is used to calculate the contact resistivity at different contact pressures, and the latter is used to calibrate the model parameters so that it is more in line with the actual stack performance.

### *2.1. The Test of Contact Resistance*

Due to the different properties of the BPP and the GDL, the fitting relationship between the contact resistance and the contact pressure is different. The contact resistance between

the BPP and the GDL of the fuel cell used in the test is measured and fitted. The fitting results can provide parameters for the multi-field coupled PEMFC model.

#### 2.1.1. Test Methods

In the test, the measuring instrument is a ST-2258C digital multifunctional four-probe tester, with a SZT-E semiconductor material resistance four-terminal test bench (Figure 1), which can measure the resistance and resistivity of chip or block semiconductors, polymers, metal samples, and other parameters. The resistivity measurement range is $0.1 \times 10^{-3}$~$20.00 \times 10^{3}$ Ω·cm, the resolution is $0.01 \times 10^{-3}$~$0.01 \times 10^{3}$ Ω·cm, and the pressure range is 0.4~6 MPa.

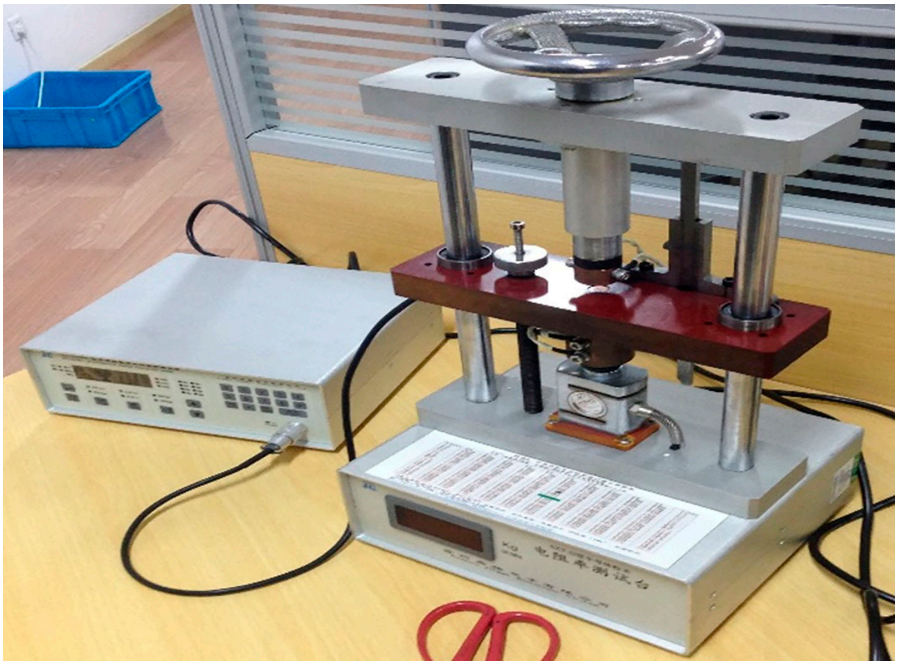

**Figure 1.** Contact resistivity tester.

In the test, the material of the BPP is graphite and the material of the GDL is Toray TGP-H 120, as shown in Table 2. The relationship between the contact resistance and the contact pressure of the BPP and the GDL at different pressures can be tested. Considering the contact pressure inside the fuel cell, the pressure variation range of the test was set as 0.5 MPa~2.0 MPa, and the corresponding resistance value is measured.

**Table 2.** The properties of the test materials.

| Material Properties | | BPP (T8-D) | GDL (TGP-H120) |
|---|---|---|---|
| coefficient of linear expansion ($10^{-6}$·$K^{-1}$) | vertical to fiber direction | 3.77 | 1.7 |
| | parallel to the fiber direction | 2.22 | 22 |
| thermal conductivity (W·$m^{-1}$·$K^{-1}$) | vertical to fiber direction | 43 | 15 |
| | parallel to the fiber direction | 32 | −0.8 |
| elastic modulus (MPa) | | 130 | 6.13 |
| Poisson's ratio | | 0.21 | 0.09 |
| specific heat capacity (J·$kg^{-1}$·$K^{-1}$) | | 880 | 711.76 |
| density (kg·$m^{-3}$) | | 1850 | 450 |

Firstly, the resistance value $R_{tot1}$ of the two BPPs and a GDL is measured as shown in Figure 2a, where the two sides are the BPPs and the middle part is the GDL. Then, the resistance value $R_{tot2}$ of a single BPP is measured as shown in Figure 2b. Finally, the

resistance value $R_{BPP}$ of the BPP and the resistance value $R_{GDL}$ of the GDL are measured via an SZT-C four-probe test bench.


(**a**) (**b**)

**Figure 2.** Test, actual picture. (**a**) The resistance test of the GDL and the BPP; (**b**) The resistance test of the BPP.

The resistance values can be divided into the sum of the bulk resistance of the BPP and the GDL and the contact resistance between the BPP and the GDL, and the BPP and the current collector plates, as shown below:

$$R_{tot} = 2R_{BPP} + R_{GDL} + 2R_{GDL/BPP} + 2R_{Au/BPP} \quad (1)$$

$$R_{tot1} = R_{BPP} + 2R_{Au/BPP} \quad (2)$$

wherein, the $R_{GDL/BPP}$ is the contact resistance between the BPP and GDL, and $R_{Au/BPP}$ is the contact resistance between the BPP and current collector plate. The contact resistance between the GDL and BPP can be obtained from Equations (1) and (2). As long as the actual contact area $A_{GDL/BPP}$ is obtained, then the contact resistivity can be obtained via Equation (3):

$$\rho_{GDL/BPP} = R_{GDL/BPP} \times A_{GDL/BPP} \quad (3)$$

2.1.2. Test Results

The contact resistance under different contact pressures can be measured using the test. The test data can be fitted via Equation (4) [37], which is helpful to obtain the contact resistance without the test, as shown below:

$$\rho_c = K \cdot p^{-m} \quad (4)$$

where $p$ is the contact pressure; $\rho_c$ is the interfacial contact resistance; and K and $m$ are the fitted parameters.

Equation (4) is a commonly used formula for the contact resistance, which is derived from empirical formulas. In this study, the relevant parameters are obtained via fitting the function in MATLAB®. The detailed test data are shown in Table 3 and the fitting parameters are shown in Table 4. The fitness is 0.9929 and the value of RMSE (Root Mean Square Error) is 0.558, which shows the fitted curve is in good agreement with the test data. The magnitude and trends are consistent with the test results of Mishra [38] and Wang [39]. The fitting parameters provide the basis for the model and can effectively improve the accuracy of the model. The error between the fitted data and the actual data are not more than 3.3%, where the error of the contact resistivity can be calculated via Equation (5):

$$\text{error rate} = \frac{|\text{contact resistivity} - \text{fitted contact resistivity}|}{\text{contact resistivity}} \times 100\% \quad (5)$$

**Table 3.** The results of the contact resistivity test.

| Contact Pressure (MPa) | Contact Resistivity (mΩ/cm$^2$) | Fitted Contact Resistivity (mΩ/cm$^2$) | Error Rate (%) |
|---|---|---|---|
| 0.511 | 41.95 | 42.42 | 1.1 |
| 0.638 | 36.56 | 37.15 | 1.6 |
| 0.765 | 33.70 | 33.33 | 1.1 |
| 0.892 | 31.26 | 30.40 | 2.7 |
| 1.019 | 28.94 | 28.07 | 3.0 |
| 1.146 | 27.06 | 26.17 | 3.3 |
| 1.273 | 24.52 | 24.57 | 0.2 |
| 1.400 | 22.95 | 23.21 | 1.1 |
| 1.527 | 21.98 | 22.04 | 0.3 |
| 1.654 | 20.63 | 21.01 | 1.8 |
| 1.781 | 19.66 | 20.10 | 2.2 |
| 1.908 | 18.71 | 19.29 | 3.1 |

**Table 4.** The fitting parameters of the contact pressure and the contact resistance.

| Parameter | Value | Units |
|---|---|---|
| K | 28.39 | mΩ·cm$^2$ |
| m | 0.5983 | |

According to the test results, the fitted curve between the contact resistivity and the contact pressure is shown in Figure 3. With the increase in contact pressure, the contact resistance and the contact resistivity decrease, and the degree of decline tends to decrease.

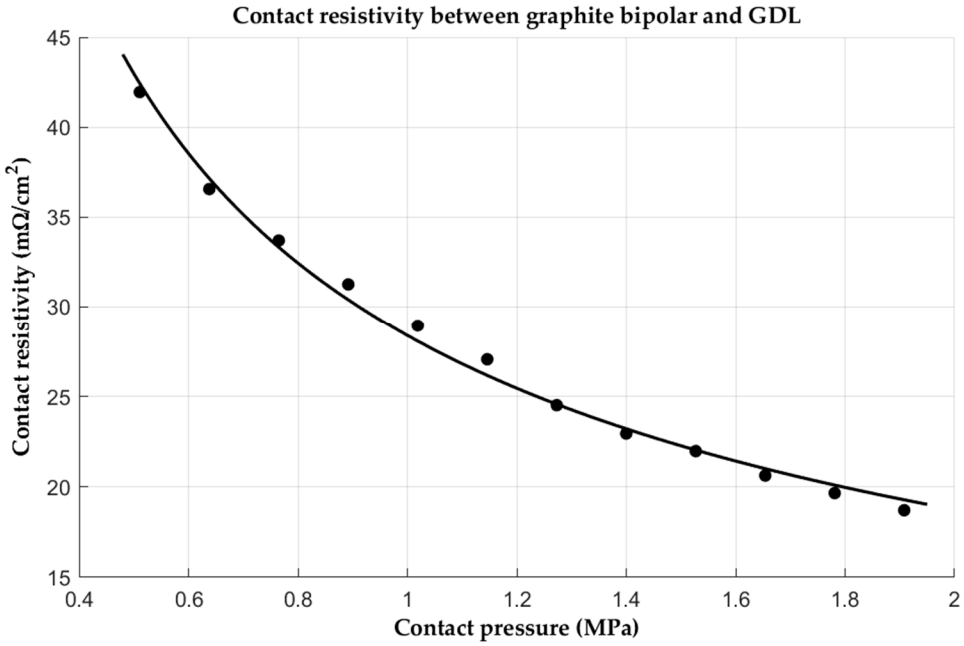


**Figure 3.** The fitted curve between the contact resistivity and the contact pressure of the GDL and the BPP.

### *2.2. Parameter Calibration*

There are many parameters that need to be set in ANSYS® and FLUENT®. The performance of the model can be closer to that of the actual stack by calibrating the parameters of the model via the polarization curve of a single cell.

2.2.1. Materials and Test Method

The test is performed with a short fuel cell stack to correct the model parameters. The short PEM fuel cell stack is composed of 15 single cells with the insulation plates, current collection plates, and endplates on both sides.

The full-dimensional cell size is 100 mm × 400 mm, and the activation area is 260 $cm^2$. The graphite bipolar plates are 100 mm × 400 mm in size; MEA (XL20120823-098) is provided by Taiwan Nan Ya PCB Corporation (New Taipei City, Taiwan). The PEM is DuPont™ Nafion® XL-100, where the effective area is 250 $cm^2$; GDL selects Toray TGP-H 120. The anode and cathode catalysts are Pt/C, where the anode Pt load of a MEA is 0.1 $mg/cm^2$, the cathode is 0.4 $mg/cm^2$, and the flow channel is a linear parallel channel.

The fuel cell test platform is Canada Greenlight G500 Test Station, which is composed of a hydrogen supply, air supply, and cooling and control subsystems. The platform can not only accurately measure and control the fuel cell stack operation parameters, such as inlet pressure, temperature, flow rate and humidity, etc., but the operating current of the fuel cell stack can also be controlled by the electronic load on the platform to simulate the vehicular working conditions, as shown in Figure 4.

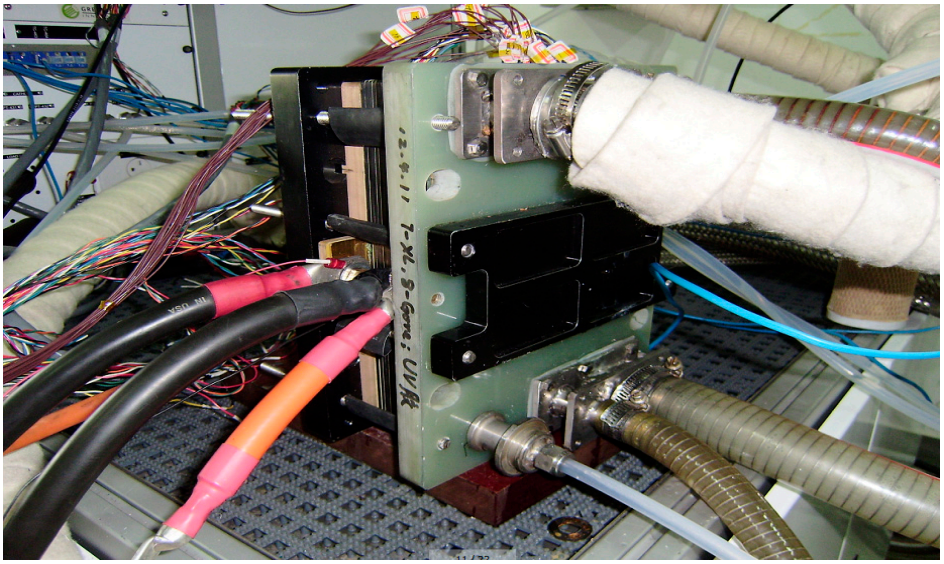

**Figure 4.** The tested fuel cell stack and the platform (The words in Figure 4 are only used for tests. There is no special meaning here).

2.2.2. The Polarization Curve of the Short Fuel Cell Stack

MEAs are fully activated and then the polarization curve is tested. The tested current range is 0~400 A, and the interval is 10 A. The working conditions of the test are described in Table 5.

**Table 5.** Test conditions.

| Parameters | Test |
|---|---|
| Hydrogen inlet pressure (kPa) | 150 |
| Air inlet pressure (kPa) | 100 |
| Stoichiometric coefficient | 1.8 |
| Hydrogen inlet humidity (%) | 0 |
| Air inlet humidity (%) | 45~60 |
| Working temperature (°C) | 75 |

Based on the working conditions, the polarization curve of the test and model with different current densities are obtained as shown in Figure 5. Some typical voltage and power data are listed in Table 6.

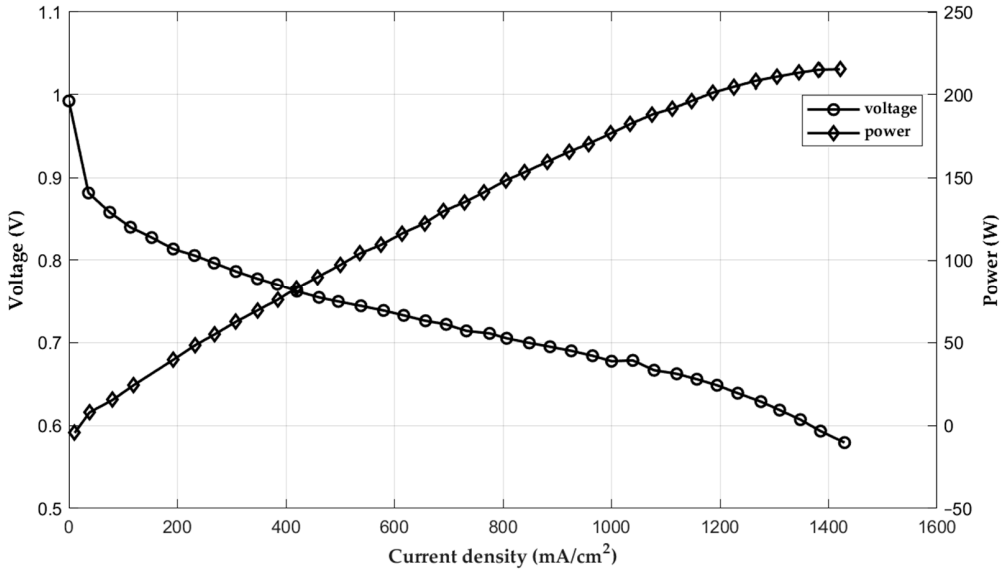


**Figure 5.** The polarization characteristic curves of the test.

**Table 6.** The test values under different current densities.

| Current Density (A/cm$^2$) | 0.1 | 0.5 | 0.8 | 1.0 | 1.2 |
|---|---|---|---|---|---|
| Test voltage (V) | 0.847 | 0.748 | 0.705 | 0.678 | 0.645 |
| Test power (W) | 22.02 | 97.24 | 146.64 | 176.28 | 201.24 |

As shown in Figure 5, with the increase in current densities, the model and test results of output voltages and power are consistent, and the V-I curve of the multi-field coupled numerical simulation is close to the test results. These test results show that the multi-field coupled model is accurate enough to simulate the PEMFC electrochemical performance for optimization.

## 3. Models Description of the Force-Temperature-Humidity Coupled Model

### *3.1. Models Description of the Force-Temperature-Humidity Coupled Model*

A single channel model of a single cell is established in this chapter. The model structure is based on the actual stack structure which is used in the test. The structural parameters of the BPP and MEA for the model and test are similar, and the main structural parameters are shown in Table 7. The material properties of the model are the same as the actual material properties, which are listed in Table 2.

**Table 7.** The dimensions of the PEMFC model.

| Dimensions | Units | Value |
|---|---|---|
| Anode BPP Height | mm | 0.8 |
| Cathode BPP Height | mm | 1.2 |
| GDL Height | mm | 0.25 |
| CL Height | mm | 0.008 |
| PEM Height | mm | 0.025 |
| Flow Channel Height | mm | 0.4 |
| Flow channel Width | mm | 1.2 |
| Single cell Width | mm | 2 |
| Length | mm | 317 |

3.1.1. The Force-Temperature Coupled Model

A PEMFC single cell is proposed which is mainly composed of BPPs, GDLs, CLs, and a PEM. Due to the structural symmetry, a 1/2 model is adopted in ANSYS® to establish the model.

The main object of the model is the contact pressure and deformation between the BPP and the GDL. So, a force-temperature coupled model can be established via the following assumptions: (1) the effect of the contact pressure on the contact resistance is concentrated between the BPPs and GDLs; (2) the CLs and PEMs are very thin in thickness, so the influence of temperature on deformation is not considered; and (3) the inelastic deformation is ignored.

The displacement load acts on the BPP upper surface as the assembly force. Due to the symmetry of the PEMFC structure, the BPP and the GDL are simplified into a translational repetitive symmetric structure. There are symmetric loads on the lower surface and the two-side surface of the structure. These loads can be seen in Figure 6.

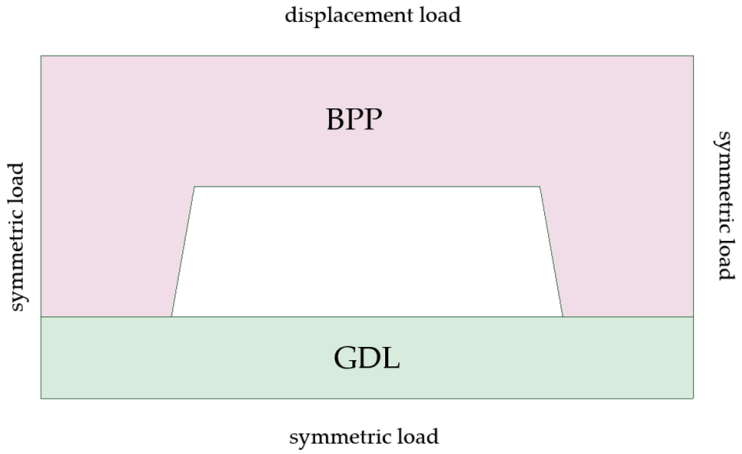


**Figure 6.** The model structures.

Under the action of assembly force, the BPP and the GDL will come into contact, and the contact behavior of the BPP and the GDL is represented via a surface-surface contact element, which is also attached to the inner side of the flow channel.

3.1.2. The Temperature-Humidity Coupled Model

The temperature-humidity coupled model established in FLUENT® is a single channel model of a single cell due to the symmetric structure, including the anode, cathode, flow channels, GDLs, CLs, and a PEM, as shown in Figure 7. The outlet of the flow channel is set as a pressure outlet for the purge value action of the fuel cell system, while the inlet of the flow channel is set as a mass flow inlet.

Hydrogen, air, and water vapor are considered in FLUENT®. The assumptions of the model are as follows: (1) all gases involved in the reaction are ideal gases; (2) the gas flow in the model is steady state; and (3) the porous medium in the model is isotropic.

The main equations used in FLUENT® are the mass conservation equation [40], the energy conservation equation [40], the momentum conservation equation [40], the current conservation equation [41], the Butler–Volmer equation [41] and the diffusion equation in the porous zone [42]. The detailed equations can be found in the above literature.

The gas behavior during the electrochemical reaction is different with the temperature and pressure, and the expressions of dynamic viscosity and the mass diffusion coefficient of each gas under different temperatures and pressures are shown in Table 8. The inputs are set to FLUENT® via UDF (user defined functions) to increase the accuracy of the simulation.

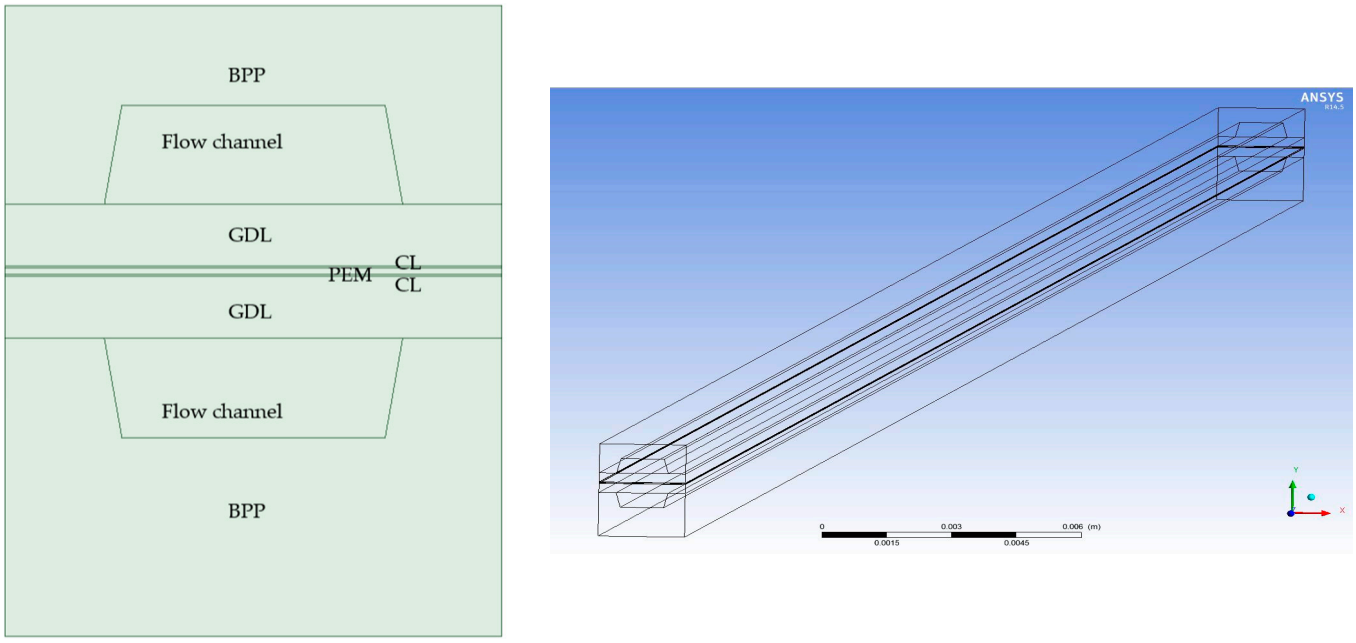


(**a**) (**b**)

**Figure 7.** The single cell structure of the temperature-humidity coupled model. (**a**) Two-dimensional structure; and (**b**) three-dimensional structure.

**Table 8.** The parameters of the temperature-humidity coupled model.

| Parameters | Expression |
|---|---|
| Hydrogen dynamic viscosity ($kg \cdot m^{-1} \cdot s^{-1}$) | $\mu_{H_2} = 3.205 \times 10^{-3}(T/298.35)^{1.5}(T+72)^{-1.0}$ |
| Oxygen dynamic viscosity ($kg \cdot m^{-1} \cdot s^{-1}$) | $\mu_{O_2} = 8.46 \times 10^{-3}(T/292.25)^{1.5}(T+127)^{-1.0}$ |
| Water dynamic viscosity ($kg \cdot m^{-1} \cdot s^{-1}$) | $\mu_{H_2O} = 7.512 \times 10^{-3}(T/291.15)^{1.5}(T+120)^{-1.0}$ |
| Hydrogen diffusion coefficient ($m^2 \cdot s^{-1}$) | $D_{H_2} = 1.055 \times 10^{-4}(T/333.15)^{1.5}(101,325/p)$ |
| Oxygen diffusion coefficient ($m^2 \cdot s^{-1}$) | $D_{O_2} = 2.652 \times 10^{-5}(T/333.15)^{1.5}(101,325/p)$ |
| Anode water diffusion coefficient ($m^2 \cdot s^{-1}$) | $D^A_{H_2O} = 1.055 \times 10^{-4}(T/333.15)^{1.5}(101,325/p)$ |
| Cathode water diffusion coefficient ($m^2 \cdot s^{-1}$) | $D^C_{H_2O} = 2.982 \times 10^{-5}(T/333.15)^{1.5}(101,325/p)$ |
| Heat capacity ($J \cdot kg^{-1} \cdot K^{-1}$) | $(C_p)_{H_2} = 14,283.$ $(C_p)_{O_2} = 919.31$ |
| Water heat capacity ($J \cdot kg^{-1} \cdot K^{-1}$) | $(C_p)_{H_2O} = 2014$ |
| Hydrogen effective thermal conductivity ($W \cdot m^{-1} \cdot K^{-1}$) | $k_{H_2} = 0.1672$ |
| Oxygen effective thermal conductivity ($W \cdot m^{-1} \cdot K^{-1}$) | $k_{O_2} = 0.0264$ |
| Water effective thermal conductivity ($W \cdot m^{-1} \cdot K^{-1}$) | $k_{H_2O} = 0.0261$ |

#### 3.1.3. The Force-Temperature-Humidity Multi-Field Coupled Model

The force-temperature coupled model and the temperature-humidity model can be integrated via the temperature distribution. In the beginning, the variation in the GDL displacement and the contact pressure on each contact element in the contact area can be obtained via the force-temperature coupled model, where the temperature is 20 °C. Secondly, Equation (6) [43] shows the influence of the GDL deformation on the GDL porosity, which can calculate the GDL porosity under deformation, as shown below:

$$\varepsilon_z = 1 - (1 - \varepsilon_0)\frac{\delta_0}{\delta_z} \tag{6}$$

where $\varepsilon_0$ is the initial porosity; $\varepsilon_z$ is the porosity under deformation; $\delta_0$ is the initial thickness; and $\delta_z$ is the thickness under deformation. The contact resistance can be obtained via the fitted curve between the contact resistivity and the contact pressure.

Furthermore, the temperature distribution of the model under the action of assembly force and internal temperature, which can be loaded into the force-temperature coupled model, can be obtained via the temperature-humidity coupled model, which has considered the porosity and the contact resistance using UDF.

After that, the error of the contact resistance and the contact pressure for this time and last time can be used as an evaluation index to illustrate the coupled effect of the model. The influence of temperature differences between the model and steady state can be ignored if the result is less than 1%, which shows the force-temperature-humidity multi-field coupled model reaching steady state. If not, we repeat the above process until the requirements are met.

Finally, the fuel cell performance and internal state can be obtained from the force-temperature-humidity coupled model after the model reaches steady state, which facilitate the optimization of the fuel cell performance.

### *3.2. Parameter Calibration*

In order to calibrate the parameters, the test conditions and simulation conditions should be the same. The simulation working conditions are designed based on the test working conditions. The working conditions of the test and model are described in Table 9.

**Table 9.** Test and Model conditions.

| Parameters | Test | Model |
|---|---|---|
| Hydrogen inlet pressure (kPa) | 150 | 120 |
| Air inlet pressure (kPa) | 100 | 100 |
| Stoichiometric coefficient | 1.8 | 1.5/2.7 |
| Hydrogen inlet humidity (%) | 0 | 0 |
| Air inlet humidity (%) | 45~60 | 60 |
| Working temperature (°C) | 75 | 75 |
| Displacement load (mm) | - | 0.07 |

Based on the working conditions, the voltage and power of the model with the different current densities are obtained, which are listed in Table 10. The polarization of the model and the test are shown in Figure 8.

**Table 10.** The test and model values under different current densities.

| Current Density (A/cm$^2$) | 0.1 | 0.5 | 0.8 | 1.0 | 1.2 |
|---|---|---|---|---|---|
| Test voltage (V) | 0.847 | 0.748 | 0.705 | 0.678 | 0.645 |
| Model voltage (V) | 0.8192 | 0.7186 | 0.6664 | 0.6371 | 0.5897 |
| Test power (W) | 22.02 | 97.24 | 146.64 | 176.28 | 201.24 |
| Model power (W) | 20.30 | 93.34 | 138.53 | 163.28 | 184.08 |
| Error rate (%) | 3.28 | 3.93 | 5.47 | 6.03 | 8.45 |

The error between the test power and the model power can be calculated via Equation (7). The results show that the error increases with the increase in current density. One of the reasons why the error at a high current density is larger is the lack of the effect of water on membrane swelling, as shown below:

$$\text{error rate} = \frac{|\text{test power} - \text{model power}|}{\text{test power}} \times 100\% \quad (7)$$

As shown in Figure 8, with the increase in current densities, the model and test results of output voltages and power are consistent, and the V-I curve of the multi-field coupled numerical simulation is close to the test results. The test results show that the multi-field coupled model is accurate enough to simulate the PEMFC electrochemical performance for optimization.

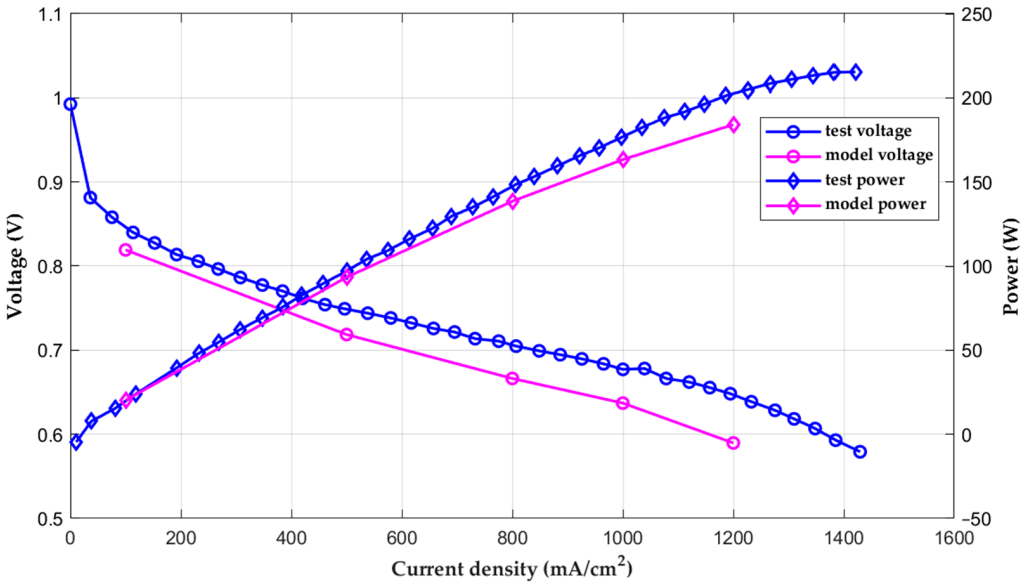


**Figure 8.** The polarization characteristic curves of the model and the test.

### *3.3. Model Validation*

To validate the PEMFC multi-field coupled model, and because the purpose mainly focuses on the performance optimization of the fuel cell voltage and its distribution and coupling of the internal parameters, the full-dimensional fuel cell stack is tested in this study.

The long fuel cell stack is composed of 200 single cells with the same insulation plates, current collection plates, endplates, etc. The end plates on both sides are steel. The fuel cell stack is assembled with four steel belts, as shown in Figure 9. The structure of the single cell in the long fuel cell stack is similar to the structure of the single cell in the short fuel cell, and the activation area of the single cell is 260 cm$^2$.

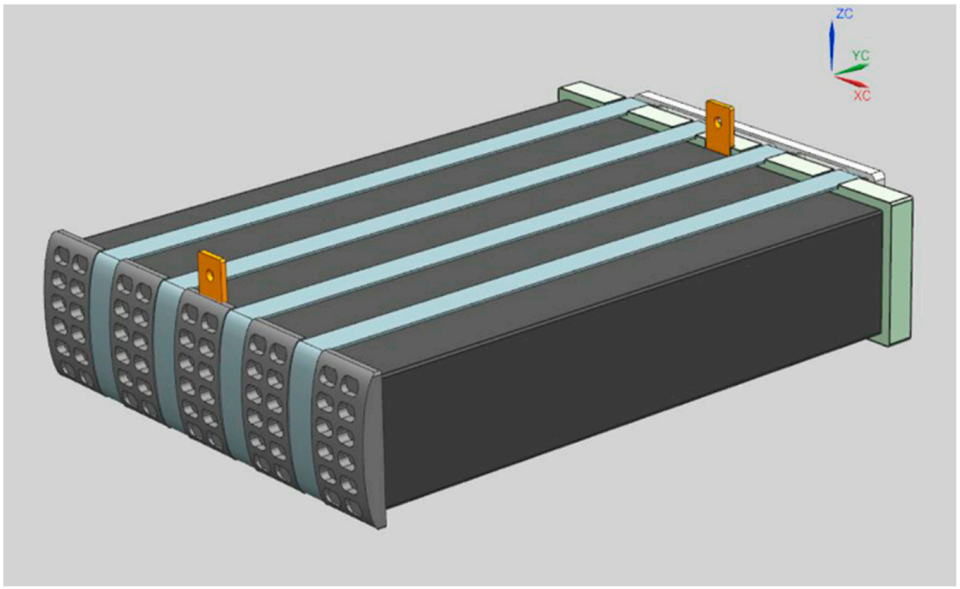


**Figure 9.** The structure of the fuel cell stack.

In this test, the MEA is also fully activated for the optimal fuel cell stack performance. The test current ranges from 0 to 400 A, and the fuel cell stack output performance at 260 A, 312 A, and 390 A is tested. The operating conditions in the test are listed in Table 11, which are identical with the established multi-fields coupled model.

**Table 11.** Operating conditions of the tested long fuel cell stack and the correspondent model.

| Current | Structure | Inlet Pressure (kPa) | Outlet Pressure (kPa) | Humidity | Inlet Temperature (°C) | Outlet Temperature (°C) |
|---|---|---|---|---|---|---|
| 260 A | Anode | 120.0 | 104.3 | 75.6 | 26.9 | 62.4 |
| | Cathode | 100.0 | 31.2 | 69.8 | 64.3 | 67.4 |
| | Coolant | 83.3 | 53.3 | / | 59.7 | 67.2 |
| 312 A | Anode | 120.0 | 110.8 | 82.4 | 27.9 | 58.4 |
| | Cathode | 100.0 | 44.4 | 77.8 | 65.3 | 71.4 |
| | Coolant | 94.3 | 61.1 | / | 58.1 | 72.1 |
| 390 A | Anode | 120.0 | 114.2 | 94.6 | 29.3 | 64.7 |
| | Cathode | 100.0 | 62.4 | 80.8 | 64.8 | 73.6 |
| | Coolant | 114 | 72 | / | 67.3 | 75.1 |

Based on the results which are listed in Table 12 with three operating currents, it can be found that test results of the long fuel cell stack are highly identical to the numerical simulation results. Under the conditions of 1.0 A/cm$^2$ (260 A), 1.2 A/cm$^2$ (312 A), and 1.5 A/cm$^2$ (390 A), the errors of the voltages are respectively 3.37%, 1.93%, and 1.56%. The errors of power are respectively 1.35%, 0.73%, and 2.85%.

**Table 12.** The results of the long fuel cell stack test.

| Current | Structure | Current Density (A/cm$^2$) | Activation Area * (cm$^2$) | Voltage * (V) | Power * (W) |
|---|---|---|---|---|---|
| 260 A | model | 1.0 | 260 | 0.654833 | 170.26 |
| | test | 0.989 | 260 | 0.667 | 172.59 |
| | error rate (%) | - | - | 3.27 | 1.35 |
| 312 A | model | 1.2 | 260 | 0.624653 | 194.89 |
| | test | 1.192 | 260 | 0.637 | 196.32 |
| | error rate (%) | - | - | 1.93 | 0.73 |
| 390 A | model | 1.5 | 260 | 0.574948 | 224.30 |
| | test | 1.489 | 260 | 0.566 | 217.90 |
| | error rate (%) | - | - | 1.56 | 2.85 |

* Here, these physical quantities are calculated on the basis of a single cell.

Although there exists a series of possible tolerance caused by the test platform and the fuel cell stack assembly, the error between the multi-field coupled model and the long full-dimensional fuel cell stack is also allowable. Therefore, the multi-field coupled model of the force-humidity-temperature co-simulated with FEA and CFD are potentials to optimize the multiple working conditions for optimal fuel cell performance.

## 4. Conclusions

In order to optimize the fuel cell electrochemical performance, the main working conditions of the fuel cell stack, such as assembly force, working temperature, and humidity and their coupled relation, are studied. Furthermore, the compression and the contact behaviors of the GDL are highlighted in this study for a high precise fuel cell performance prediction model. Based on this, a force-temperature coupled model of fuel cells with FEA and a temperature-humidity coupled model with CFD are established. Based on the relationship between the contact pressure and the contact resistance obtained via the experiments, the force-temperature-humidity multi-field coupled numerical model is co-simulated considering the contact resistance and the GDL porosity. Then, the short fuel cell stack test with 15 cells is used to correct the model parameters, and the long fuel cell stack test with 200 cells is used to validate the accuracy of the model.

The main conclusions are as follows:

(1) The compression ratio of the GDL has a great influence on its porosity and contact resistance, whose relationship is completive for the electron transportation and fuel supply, and they are necessary to be considered in the fuel cell performance prediction and optimization model to balance the ohmic losses and concentration losses.
(2) The structural analysis of the GDL contact resistance with FEA considering the thermo-force coupling, and the electrochemical analysis of the GDL compression with CFD considering the thermo-hydrate coupling, are potentials to reveal the fuel cell stack performance.
(3) Under the operating conditions of 260 A, 312 A, and 390 A in the long fuel cell stack test of 200 cells, the voltage error between the test and the model is a maximum of 3.27%, and the power error between the test and the model is maximum of 2.85%, which indicates that this model is precise enough to predict and optimize the fuel cell performance.

This study establishes the force-temperature-humidity coupled model of fuel cells to predict the performance of fuel cells under different assembly forces, which has been validated via tests. This model is convenient to observe the influence of various parameters on the fuel cell performance, which is helpful to optimize the parameters and analyze the internal state of fuel cells.

**Author Contributions:** Conceptualization, Z.Z. and K.L.; methodology, Z.Z. and Z.C.; software, Z.C. and X.Z.; validation, Z.Z., Z.C. and C.Z.; resources, Z.Z. and T.Z.; writing—original draft preparation, Z.Z. and Z.C.; writing—review and editing, Z.Z. and X.Z.; project administration, Z.Z. and T.Z.; funding acquisition, Z.Z. All authors have read and agreed to the published version of the manuscript.

**Funding:** This research was funded by the Natural Science Foundation of Shanghai, grant number 22ZR1466800.

**Institutional Review Board Statement:** Not applicable.

**Informed Consent Statement:** Not applicable.

**Data Availability Statement:** Not applicable.

**Conflicts of Interest:** The authors declare no conflict of interest.

## References

1. IEA. Greenhouse Gas Emissions from Energy Data Explorer. Available online: https://www.iea.org/data-and-statistics/data-tools/greenhouse-gas-emissions-from-energy-data-explorer (accessed on 25 May 2023).
2. Li, W.; Bao, L.; Li, Y.; Si, H.; Li, Y. Assessing the transition to low-carbon urban transport: A global comparison. *Resour. Conserv. Recycl.* **2022**, *180*, 106179. [CrossRef]
3. Liu, Y.; Guo, H.; Ouyang, X. Development Status and Future Prospects of Hydrogen Fuel Cell Technology. *Eng. Sci.* **2021**, *23*, 162–171. [CrossRef]
4. Wang, C.; Wang, S.B.; Zhang, J.B.; Li, J.Q.; OuYang, M.G.; Wang, J.L. The Key Materials and Components for Proton Exchange Membrane Fuel Cell. *Prog. Chem.* **2015**, *27*, 310–320. [CrossRef]
5. Song, K.; Wang, Y.M.; Ding, Y.H.; Xu, H.J.; Mueller-Welt, P.; Stuermlinger, T.; Bause, K.; Ehrmann, C.; Weinmann, H.W.; Schaefer, J.; et al. Assembly techniques for proton exchange membrane fuel cell stack: A literature review. *Renew. Sustain. Energy Rev.* **2022**, *153*, 28. [CrossRef]
6. Zhang, J.; Hu, Y.; Han, C.; Zhang, H. Stress response and contact behavior of PEMFC during the assembly and working condition. *Int. J. Hydrogen Energy* **2021**, *46*, 30467–30478. [CrossRef]
7. Xia, L.; Ni, M.; He, Q.; Xu, Q.; Cheng, C. Optimization of gas diffusion layer in high temperature PEMFC with the focuses on thickness and porosity. *Appl. Energy* **2021**, *300*, 117357. [CrossRef]
8. Shangguan, X.; Li, Y.; Qin, Y.; Cao, S.; Zhang, J.; Yin, Y. Effect of the porosity distribution on the liquid water transport in the gas diffusion layer of PEMFC. *Electrochim. Acta* **2021**, *371*, 137814. [CrossRef]
9. Atyabi, S.A.; Afshari, E.; Wongwises, S.; Yan, W.-M.; Hadjadj, A.; Shadloo, M.S. Effects of assembly pressure on PEM fuel cell performance by taking into accounts electrical and thermal contact resistances. *Energy* **2019**, *179*, 490–501. [CrossRef]
10. Zhang, S.; Dai, H.; Yuan, H.; Ming, P.; Wei, X. Sensibility Study on Electrochemical Impedance of Proton Exchange Membrane Fuel Cell. *J. Mech. Eng.* **2021**, *57*, 40–51.
11. Bhosale, A.C.; Rengaswamy, R. Interfacial contact resistance in polymer electrolyte membrane fuel cells: Recent developments and challenges. *Renew. Sustain. Energy Rev.* **2019**, *115*, 109351. [CrossRef]

12. Ouaidat, G.; Cherouat, A.; Kouta, R.; Chamoret, D. Numerical modeling of the mechanical behavior of proton exchange membrane fuel cell performance: Design of experiment study and optimization. *Int. J. Hydrogen Energy* **2020**, *45*, 25210–25226. [CrossRef]
13. Huo, W.M.; Wu, P.; Xie, B.; Du, Q.; Liang, J.Q.; Qin, Z.G.; Zhang, G.B.; Sarani, I.; Xu, W.Z.; Liu, B.H.; et al. Elucidating non-uniform assembling effect in large-scale PEM fuel cell by coupling mechanics and performance models. *Energy Convers. Manag.* **2023**, *277*, 14. [CrossRef]
14. Lin, J.; Wu, P.; Dai, H.; Qiu, Y.; Zhang, J. Intelligent optimization of clamping design of PEM fuel cell stack for high consistency and uniformity of contact pressure. *Int. J. Green Energy* **2022**, *19*, 95–108. [CrossRef]
15. Barzegari, M.M.; Ghadimi, M.; Momenifar, M. Investigation of contact pressure distribution on gas diffusion layer of fuel cell with pneumatic endplate. *Appl. Energy* **2020**, *263*, 114663. [CrossRef]
16. Qiu, Y.; Wu, P.; Miao, T.; Liang, J.; Jiao, K.; Li, T.; Lin, J.; Zhang, J. An Intelligent Approach for Contact Pressure Optimization of PEM Fuel Cell Gas Diffusion Layers. *Appl. Sci.* **2020**, *10*, 4194. [CrossRef]
17. Irmscher, P.; Qui, D.; Janssen, H.; Lehnert, W.; Stolten, D. Impact of gas diffusion layer mechanics on PEM fuel cell performance. *Int. J. Hydrogen Energy* **2019**, *44*, 23406–23415. [CrossRef]
18. Peng, L.; Shao, H.; Qiu, D.; Yi, P.; Lai, X. Investigation of the non-uniform distribution of current density in commercial-size proton exchange membrane fuel cells. *J. Power Sources* **2020**, *453*, 227836. [CrossRef]
19. Zhang, T.; Li, J.; Li, Q.; Yu, M.; Sun, H. Combination effects of flow field structure and assembly force on performance of high temperature proton exchange membrane fuel cells. *Int. J. Energy Res.* **2021**, *45*, 7903–7917. [CrossRef]
20. Toghyani, S.; Nafchi, F.M.; Afshari, E.; Hasanpour, K.; Baniasadi, E.; Atyabi, S.A. Thermal and electrochemical performance analysis of a proton exchange membrane fuel cell under assembly pressure on gas diffusion layer. *Int. J. Hydrogen Energy* **2018**, *43*, 4534–4545. [CrossRef]
21. Shi, L.; Xu, S.; Liu, J. Influences of assembly pressure and flow channel size on performances of proton exchange membrane fuel cells based on a multi-model. *Int. J. Hydrogen Energy* **2022**, *47*, 7902–7914. [CrossRef]
22. Bouziane, K.; Khetabi, E.M.; Lachat, R.; Zamel, N.; Meyer, Y.; Candusso, D. Impact of cyclic mechanical compression on the electrical contact resistance between the gas diffusion layer and the bipolar plate of a polymer electrolyte membrane fuel cell. *Renew. Energy* **2020**, *153*, 349–361. [CrossRef]
23. Zhang, M.F.; Liu, Y.W.; Qin, Y.Z.; Zhang, T.; Han, X.; Wang, Y.F. Effects of membrane swelling on structural deformation and performance of proton exchange membrane fuel cell. *Int. J. Green Energy* **2022**, 1–12. [CrossRef]
24. Xiong, S.S.; Wu, Z.K.; Li, W.; Li, D.Z.; Zhang, T.; Lan, Y.; Zhang, X.X.; Ye, S.Y.; Peng, S.H.; Han, Z.Y.; et al. Improvement of Temperature and Humidity Control of Proton Exchange Membrane Fuel Cells. *Sustainability* **2021**, *13*, 10578. [CrossRef]
25. Rasha, L.; Cho, J.I.S.; Millichamp, J.; Neville, T.P.; Shearing, P.R.; Brett, D.J.L. Effect of reactant gas flow orientation on the current and temperature distribution in self-heating polymer electrolyte fuel cells. *Int. J. Hydrogen Energy* **2021**, *46*, 7502–7514. [CrossRef]
26. Wang, Y.; Zhou, C.; Zou, J.; Feng, Q.; Liao, J.; Xing, S.; Zhao, C.; Fan, J.; Zeng, L.; Li, H.; et al. Uncoupling Characteristics of Temperature and Relative Humidity Distribution in a Commercial-Size Polymer Electrolyte Membrane Fuel Cell. *J. Energy Eng.* **2020**, *146*, 04020052. [CrossRef]
27. Shen, J.; Zeng, L.; Tu, Z.; Liu, Z.; Liu, W. Numerical Investigation of Temperature Distribution of Proton Exchange Membrane Fuel Cells at High Current Density. *J. Porous Media* **2019**, *22*, 813–829. [CrossRef]
28. Tas, M.; Elden, G. Three-dimensional and anisotropic numerical analysis of a PEM fuel cell. *Int. J. Hydrogen Energy* **2022**, *47*, 19758–19771. [CrossRef]
29. Chugh, S.; Chaudhari, C.; Sonkar, K.; Sharma, A.; Kapur, G.S.; Ramakumar, S.S.V. Experimental and modelling studies of low temperature PEMFC performance. *Int. J. Hydrogen Energy* **2020**, *45*, 8866–8874. [CrossRef]
30. Xia, R.; Zhou, H.; Wu, R.; Wu, W.-P. Nanoindentation Investigation of Temperature Effects on the Mechanical Properties of Nafion® 117. *Polymers* **2016**, *8*, 344. [CrossRef]
31. Zhang, Z.; Zhang, J.; Shi, L.; Zhang, T. A Study of Contact Pressure with Thermo-Mechanical Coupled Action for a Full-Dimensional PEMFC Stack. *Sustainability* **2022**, *14*, 8593. [CrossRef]
32. Tang, J.; Zou, H.; Zhang, Z.; Zhang, T. Stress Analysis of Membrane Electrode Assembly of Automotive Proton Exchange Membrane Fuel Cell under Alternating Temperature Conditions. *Automob. Technol.* **2020**, *4*, 16–21.
33. Liu, W.; Qiu, D.; Peng, L.; Yi, P.; Lai, X. Mechanical degradation of proton exchange membrane during assembly and running processes in proton exchange membrane fuel cells with metallic bipolar plates. *Int. J. Energy Res.* **2020**, *44*, 8622–8634. [CrossRef]
34. Bograchev, D.; Gueguen, M.; Grandidier, J.; Martemianov, S. Stress and plastic deformation of MEA in running fuel cell. *Int. J. Hydrogen Energy* **2008**, *33*, 5703–5717. [CrossRef]
35. Mehrtash, M.; Tari, I.; Yesilyurt, S. Numerical modeling of visco-elasto-plastic hygro-thermal stresses and the effects of operating conditions on the mechanical degradation of PEFC membranes. *J. Power Sources* **2018**, *396*, 164–174. [CrossRef]
36. Ouaidat, G.; Cherouat, A.; Kouta, R.; Chamoret, D. Study of the effect of mechanical uncertainties parameters on performance of PEMFC by coupling a 3D numerical multiphysics model and design of experiment. *Int. J. Hydrogen Energy* **2022**, *47*, 23772–23786. [CrossRef]
37. Zhou, P.; Wu, C.W.; Ma, G.J. Contact resistance prediction and structure optimization of bipolar plates. *J. Power Sources* **2006**, *159*, 1115–1122. [CrossRef]
38. Mishra, V.; Yang, F.; Pitchumani, R. Measurement and Prediction of Electrical Contact Resistance between Gas Diffusion Layers and Bipolar Plate for Applications to PEM Fuel Cells. *J. Fuel Cell Sci. Technol.* **2004**, *1*, 2–9. [CrossRef]

39. Wang, H. Stainless steel as bipolar plate material for polymer electrolyte membrane fuel cells. *J. Power Sources* **2003**, *115*, 243–251. [CrossRef]
40. Kerkoub, Y.; Benzaoui, A.; Haddad, F.; Ziari, Y.K. Channel to rib width ratio influence with various flow field designs on performance of PEM fuel cell. *Energy Convers. Manag.* **2018**, *174*, 260–275. [CrossRef]
41. Carcadea, E.; Ismail, M.S.; Bin Ingham, D.; Patularu, L.; Schitea, D.; Marinoiu, A.; Ion-Ebrasu, D.; Mocanu, D.; Varlam, M. Effects of geometrical dimensions of flow channels of a large-active-area PEM fuel cell: A CFD study. *Int. J. Hydrog. Energy* **2021**, *46*, 13572–13582. [CrossRef]
42. Azarafza, A.; Ismail, M.S.; Rezakazemi, M.; Pourkashanian, M. Comparative study of conventional and unconventional designs of cathode flow fields in PEM fuel cell. *Renew. Sustain. Energy Rev.* **2019**, *116*, 17. [CrossRef]
43. Yan, X.; Lin, C.; Zheng, Z.; Chen, J.; Wei, G.; Zhang, J. Effect of clamping pressure on liquid-cooled PEMFC stack performance considering inhomogeneous gas diffusion layer compression. *Appl. Energy* **2020**, *258*, 114073. [CrossRef]